SCIENTIFIC REPORTS

OPEN

SUBJECT AREAS:
ELECTRONIC PROPERTIES AND MATERIALS
SEMICONDUCTORS
CONDENSED-MATTER PHYSICS
CHEMICAL PHYSICS

Received
17 July 2012

Accepted
26 November 2012

Published
13 December 2012

Correspondence and requests for materials should be addressed to Y.D. (daiy60@sina.com)

Realization of tunable Dirac cone and insulating bulk states in topological insulators $(Bi_{1-x}Sb_x)_2Te_3$

Chengwang Niu, Ying Dai, Yingtao Zhu, Yandong Ma, Lin Yu, Shenghao Han & Baibiao Huang

School of Physics, State Key Laboratory of Crystal Materials, Shandong University, Jinan 250100, People's Republic of China.

The bulk-insulating topological insulators with tunable surface states are necessary for applications in spintronics and quantum computation. Here we present theoretical evidence for modulating the topological surface states and achieving the insulating bulk states in solid-solution $(Bi_{1-x}Sb_x)_2Te_3$. Our results reveal that the band inversion occurs in $(Bi_{1-x}Sb_x)_2Te_3$, indicating the non-triviality across the entire composition range, and the Dirac point moves upwards till it lies within the bulk energy gap accompanying the increase of Sb concentration x. In addition, with increasing x, the formation of prominent native defects becomes much more difficult, resulting in the truly insulating bulk. The solid-solution system is a promising way of tuning the properties of topological insulators and designing novel topologically insulating devices.

The recently discovered topological insulator (TI) is a novel state of quantum matter and is characterized by time-reversal-symmetric gapless topological surface states, which appear within the bulk energy gap[1–3]. The key ingredient for creating the TI phase is spin-orbit coupling (SOC), and the strong SOC due to the heavy elements can inverse the band characters of the valence band and conduction band[4,5]. By now, TI has been at the core of a very active research area due to their exotic physical properties and potential technological applications. The bulk-insulating TI with tunable surface state is necessary and important for applications in spintronics and quantum computation. Recently, a class of strong TIs (Bi_2Se_3, Bi_2Te_3, and Sb_2Te_3) has been predicted[5] and demonstrated[6–8], and has attracted much interest due to their relatively large bulk band gaps and a single Dirac cone at the Γ point of the Brillouin zone[9–15]. However, there are some challenges remain that if binary TIs Bi_2Se_3, Bi_2Te_3, and Sb_2Te_3 are to become functional components of electronic devices. Chief among them is the unacceptably high bulk conductivity introduced by the strong defect doping (e.g., anion vacancy and antisite defects)[16]. In addition, for Bi_2Te_3, the Dirac point of the (111) surface lies below the Fermi level and is buried in the bulk valence bands, which is a potential source for scattering between the surface and bulk states[5,12]. Substantial efforts involving nanostructuring[17], chemical doping[16,18,19], and electrical gating[20–23] have been try to modulate their electronic structure, but limited progress has been made to solve the problems.

Recently, it has been shown that solid-solution, which has a similar structure to its parent compounds, is a powerful approach for engineering the electronic structure of TIs[24–29]. A topological phase transition from a normal to a topological insulator is observed in $TlBi(S_{1-x}Se_x)_2$ by changing the S/Se ratios[24,25]. While for $(Bi_{1-x}Sb_x)_2Te_3$, the topological surface states maintain over the entire Bi/Sb ratios x with the reducing of the bulk carrier density and realization of the truly insulating bulk[26,27]. This paves a new route to achieving novel devices based on topological insulators. However, the mechanism of the robustness of topological property and the factors that affect the decrease of bulk carrier density in $(Bi_{1-x}Sb_x)_2Te_3$ remain unclear. In addition, so far, the unique band inversion in $(Bi_{1-x}Sb_x)_2Te_3$ has not been observed experimentally[26,27]. Therefore, in the present work, to address exactly these questions and show the band inversion, we explore the electronic characters of $(Bi_{1-x}Sb_x)_2Te_3$ via the first-principles electronic structure calculations. We identify that both the SOC strength and lattice parameters can be effectively tuned by effectively varying the fraction of Bi and Sb. The effects of the SOC strength and lattice parameters on the band inversion, topologic surface states and formation energies of native defects are investigated. The results provide a way to tune the properties of topological insulators and are helpful to design novel topologically insulating devices.

Results

Crystal structure of $(Bi_{1-x}Sb_x)_2Te_3$. The advantage of this system is that Bi_2Te_3 and Sb_2Te_3 share the same crystal structure[26,27] with the rhombohedral setting for the primitive cell and hexagonal setting for the conventional cell. Hence, for the bulk investigation, both a 40-atom 2×2×2 supercell with rhombohedral setting and a 15-atom conventional cell with hexagonal setting (**Fig. 1a**)[30] are used. We determine the lattice constants of the solid-solution $(Bi_{1-x}Sb_x)_2Te_3$ as follows. The most stable configuration of $(Bi_{1-x}Sb_x)_2Te_3$ at a given Sb concentration *x*, from 0 to 1 by a step of 1/6 for 15-atom case and a step of 0.125 for 40-atom case, is searched through an exhaustive search (see Supplemental Information) at each level of *x* and determined through the cohesive energies calculations:

$$E_{coh} = -\frac{E_{solid} - \sum_{A} N_A E_A^{isolated}}{N_{F.U.}}. \qquad (1)$$

Where *A* (*A* = Bi, Sb, and Te) represents different atoms of the solid solution, N_A the number of *A* atoms, $N_{F.U.}$ the number of formula units, and $E_A^{isolated}$ the energies of isolated *A* atoms. For the 15-atom and 40-atom cases, $N_{F.U.} = 3$ and $N_{F.U.} = 8$, respectively. The total energies, lattice parameters, and geometry structures of determined most stable configurations are given in Supplementary Information. The cohesive energies E_{coh} for both 15-atom and 40-atom cases, as shown in **Figs. 2a** and **b**, show a nearly linear variation versus Sb concentration *x*, which unveils that there is no driving force for phase segregation. **Figs. 2c** and **d** show the lattice parameters of the most stable configurations as a function of Sb concentration x for 15-atom and 40-atom cases, respectively. The lattice parameters, for both cases, vary linearly and agree well with the Vegard's Law[31], $a((Bi_{1-x}Sb_x)_2Te_3) = (1-x)a(Bi_2Te_3) + xa(Sb_2Te_3)$, which is ascribed to the small lattice mismatch of parent compounds Bi_2Te_3 and Sb_2Te_3, demonstrating that the $(Bi_{1-x}Sb_x)_2Te_3$ are ideal to form with arbitrary x.

Electronic structures of $(Bi_{1-x}Sb_x)_2Te_3$. The topological insulators Bi_2Te_3 and Sb_2Te_3, as distinct from normal insulators, are band insulators with band invention driven by strong SOC[5]. To get a better understanding of the inversion, the projections of the lowest-conduction band of $(Bi_0Sb_1)_2Te_3$ at Γ point on Sb and Te p_z orbital versus the relative SOC strength λ/λ_0 are plotted in **Fig. 2e**. For week relative SOC strength, $\lambda/\lambda_0 < 0.68$, it is mainly coming from the Sb p_z orbital. The SOC forces a particular relation between the spin and orbital angular momentum, which leads to a level repulsion that pushing down the Sb p_z orbital and pushing up the Te p_z orbital, resulting in the two orbitals reverse when the relative SOC is strong enough ($\lambda/\lambda_0 = 0.68$), namely, band inversion occurs and the system twists into the topological insulator phase through a topological quantum phase transition. For the solid-solution $(Bi_{1-x}Sb_x)_2Te_3$, **Fig. 2f** shows the projections of the lowest-conduction band at Γ point as a function of the Sb concentration *x*. The lowest-conduction band at Γ point almost comes from the p_z orbital of Te atoms over the entire range of x from 0 to 1, indicating that the SOC of $(Bi_{1-x}Sb_x)_2Te_3$ is strong enough to inverse the band and the topological insulator phase remains for $(Bi_{1-x}Sb_x)_2Te_3$ with $0 \le x \le 1$, which agrees with the experimentally observation that the topological surface states are shown to exit with $0 \le x \le 1$[26,27].

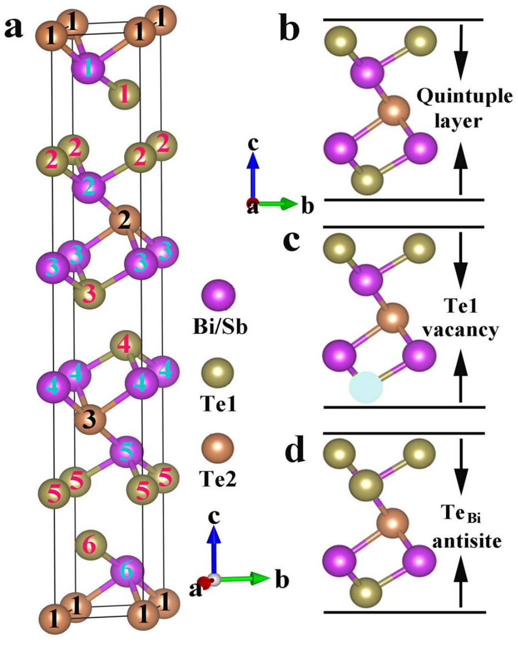

Figure 1 | Crystal structure. (a) The hexagonal conventional unit cell of $(Bi_{1-x}Sb_x)_2Te_3$, and (b) side view of the quintuple layer structure of perfect bulk, (c) Te1 vacancy, and (d) Te_{Bi} antisite. Numbers in panel (a) are the possibility sites of native point defects.

The calculated band structures of $(Bi_{1-x}Sb_x)_2Te_3$ on the (111) surface with five QLs[27] are shown in **Fig. 3**. For both end members $(Bi_1Sb_0)_2Te_3$ and $(Bi_0Sb_1)_2Te_3$, as shown in **Figs. 3a** and **b**, the topological surface states form a single Dirac cone at the Γ point, which is consistent with the previous reported results[5]. However, the shapes of their Dirac cones are significantly different. **Fig. 4a** shows the three-dimensional upper Dirac cone around the Γ point of the $(Bi_1Sb_0)_2Te_3$ (111) surfaces. Similar to the previous experiment[7] and theory[5,32,33], the ideal circular constant-energy contours, centered at the Γ point, appear below a critical energy, but the Dirac cone is significantly warped above this critical energy. For the lower Dirac cone of $(Bi_1Sb_0)_2Te_3$, as shown in **Figs. 3a**, **4a**, and **4c**, it is concave and the Dirac point is buried in the bulk valence band, making it cannot be accessed by transport experiment and opening the electron scattering channel from surface states to bulk continuum states, while $(Bi_0Sb_1)_2Te_3$ shows an ideal 'x'-shaped Dirac point with the Fermi level passes through the Dirac point (**Figs. 3b**, **4b**, and **4d**). To address the mechanism of the defining properties of the striking topological surface states vary systematically with the Bi/Sb ratios, which leads to a series of new TIs[26,27], we perform calculations for the band structures of five QLs $(Bi_1Sb_0)_2Te_3$ with rescaled SOC strength shown in **Figs. 3c**. It can be seen that with decreasing λ/λ_0 (equivalent to x increasing), the Dirac fermion velocity v_D ($v_D = \varepsilon/\hbar k$) increases accompanied the slope of the upper Dirac cone becomes steeper. Meanwhile, as shown in **Fig. 3d**, the Dirac point moves upward, resulting in the distance between the Dirac point and the Fermi level decreasing. These follow the experimental results very well[27]. With the increase of Sb concentration x, the SOC strength reduces due to that of Sb is weaker than Bi by a factor of 3. Therefore, the weaker SOC strength is the key ingredient for the change brought about by the increasing weight of the Sb when the change in lattice parameters can be neglected (inset of **Fig. 3a**). Consequently, it can be easily understand why Bi_2Se_3 and Sb_2Te_3 possess the ideal Dirac cone while Bi_2Te_3 not.

Suppression of bulk defects in $(Bi_{1-x}Sb_x)_2Te_3$. The pure Bi_2Te_3 family is expected to be undoped insulator[5], however, the currently available samples always show conductive bulk states owing to defect-induced excess carries[6,7,16], and the unacceptably high bulk conductivity is the most challenging problem that prevent the TIs to become functional components of electronic devices. The following results show the solid-solution $(Bi_{1-x}Sb_x)_2Te_3$ can effectively eliminate the unwanted defects and reduce the bulk carrier density. To show this, it is necessary to look at the formation energy, ie., the energy cost of creating the defect, and that of a charge neutral defect is given by[34]

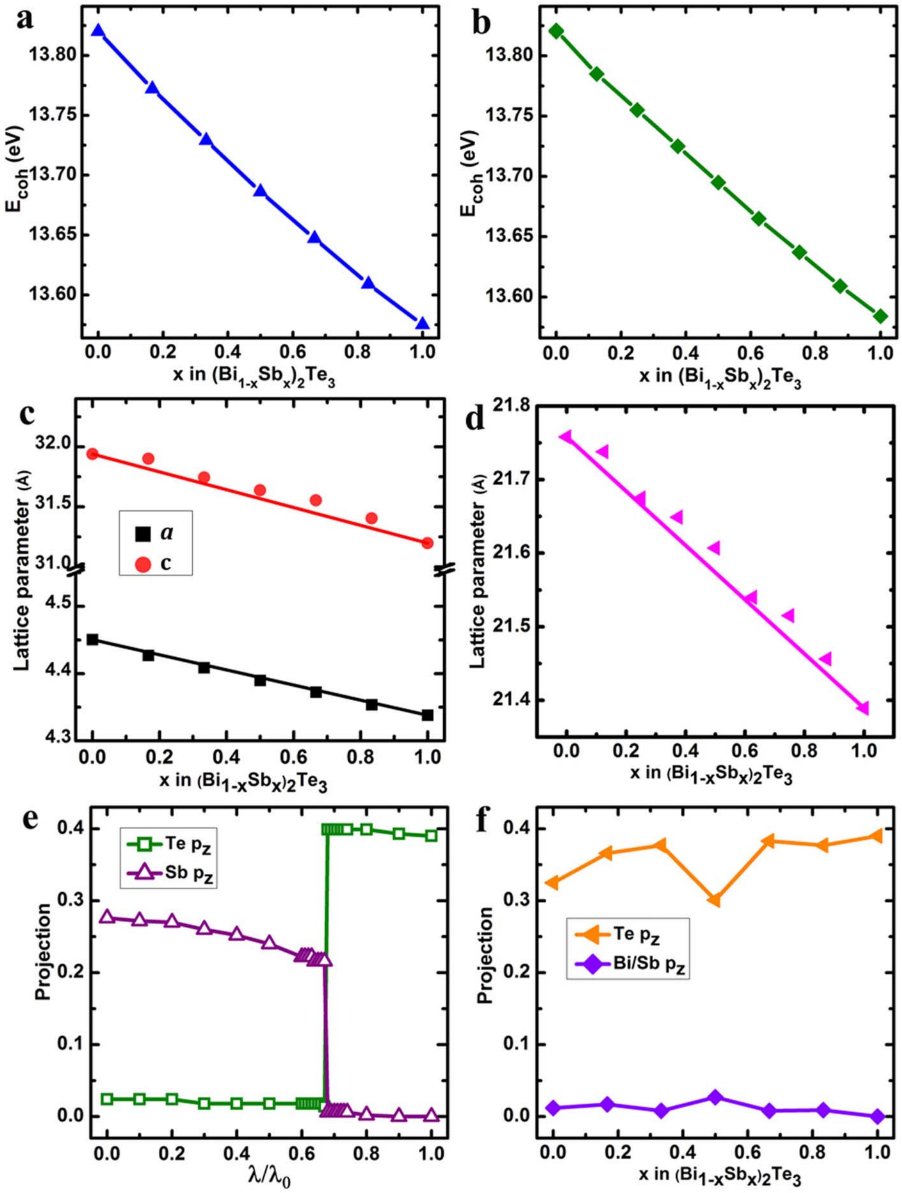

Figure 2 | Cohesive energies, lattice parameters, and projection of the lowest-conduction band. Cohesive energies per formula unit of the most stable configurations of (a) 15-atom and (b) 40-atom $(Bi_{1-x}Sb_x)_2Te_3$ at each x, and the lattice parameters of $(Bi_{1-x}Sb_x)_2Te_3$ with (c) 15-atom and (d) 40-atom plotted as a function of the Sb content x. The solid lines represent the lattice parameters calculated from Vegard's law. (e) and (f) Projection of the lowest-conduction band at Γ point on Te and Sb (Bi) p_z orbital as functions of the SOC strength (λ_0 is the actual SOC strength) with x = 1 and the Sb content x, respectively.

$$E_f = E(defect) - E(bulk) - \sum_i \Delta n_i \mu_i, \qquad (2)$$

where *E(defect)* and *E(bulk)* are the total energies of the system with and without defects. Δn_i is the change in the number of atom *i* (*i* = *Bi, Sb,* and *Te*), and μ_i is the chemical potential of the corresponding atom. The formation of a point defect depends on the growth or annealing conditions, which can be expressed by the chemical potentials, such as for Bi and Te, in thermodynamic equilibrium, the Te-rich condition corresponds to the chemical potential of Te (μ_{Te}) set to that of bulk Te, whereas the Te-poor condition corresponds to μ_{Te} is taken as $\mu_{Te} = (\mu^{bulk}_{Bi_2Te_3} - 2\mu_{Bi})/3$, with $\mu^{bulk}_{Bi_2Te_3}$ and μ_{Bi} equal to the total energy of per formula bulk Bi_2Te_3 and bulk Bi, respectively.

The most prominent defects in Bi_2Te_3 family are vacancies and antisite defects on the Bi(Sb), Te1(Se1), and Te2(Se2) sublattices. For $(Bi_1Sb_0)_2Te_3$, the natural samples are n-type semiconductors, mainly owing to the Te vacancies (V_{Te1} and V_{Te2}) (**Fig. 1c**), or the Te_{Bi} antisite defects, ie., by replacement of Bi atoms by Te atoms (**Fig. 1d**)[7,27,35], while for $(Bi_0Sb_1)_2Te_3$, the natural samples are p-type semiconductors due to the hole type carriers induced by Sb_{Te} antisite defect[30]. Firstly, different sites of defects are considered. **Table 1** summarizes the formation energies of Te vacancies and the Te_{Bi} antisite defects in 15-atom $(Bi_1Sb_0)_2Te_3$. Similar to the previous studies[30,35], the formation energies for all the defects (V_{Te1}, V_{Te2}, and Te_{Bi}) are found to be strongly dependent on the sites of defects, and the formation energies of vacancies on the Te1 sites (V_{Te1}) are lower than that for vacancies on the Te2 sites (V_{Te2}). The lower vacancy formation energy of V_{Te1} may be result from the weak van der Waals interaction between quintuple layers[5]. V_{Te1} has the higher formation energies at the Te-rich condition than that at the Te-poor condition, namely, the Te-rich limit is needed to reduce the

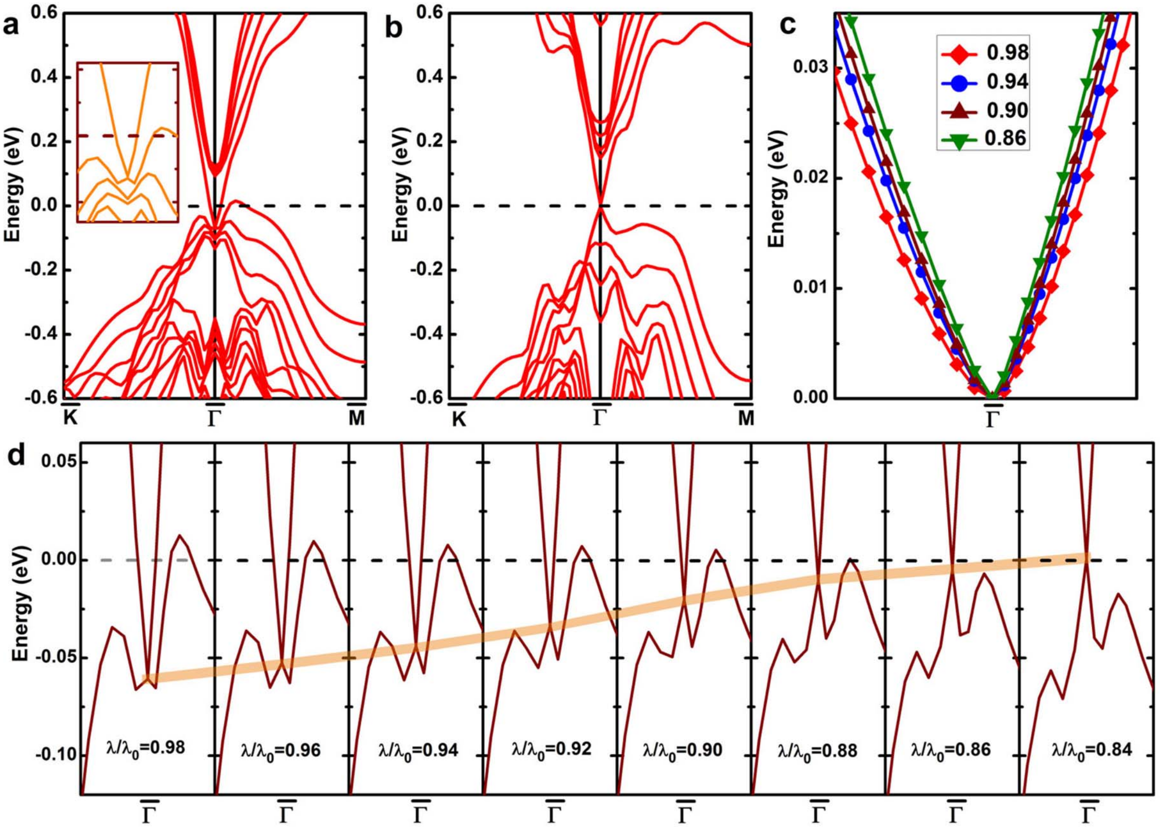

Figure 3 | **Surface states.** The band structures calculated for the 5QLs $(Bi_{1-x}Sb_x)_2Te_3$ with (a) $x = 0$ and (b) $x = 1$. (c) and (d) The evolution of the Dirac cone with different SOC strength λ/λ_0 (λ_0 is the actual SOC strength) for $(Bi_1Sb_0)_2Te_3$. The highest occupied and the lowest unoccupied bands are plotted to clearly show the evolutions. The bottom of the conduction band at Γ point is explicitly aligned to 0 eV in panel (c). The inset in panel (a) shows the zoomed-in view of band for $(Bi_1Sb_0)_2Te_3$ with the lattice parameters of $(Bi_0Sb_1)_2Te_3$. The Fermi level is indicated by the dashed line at 0 eV.

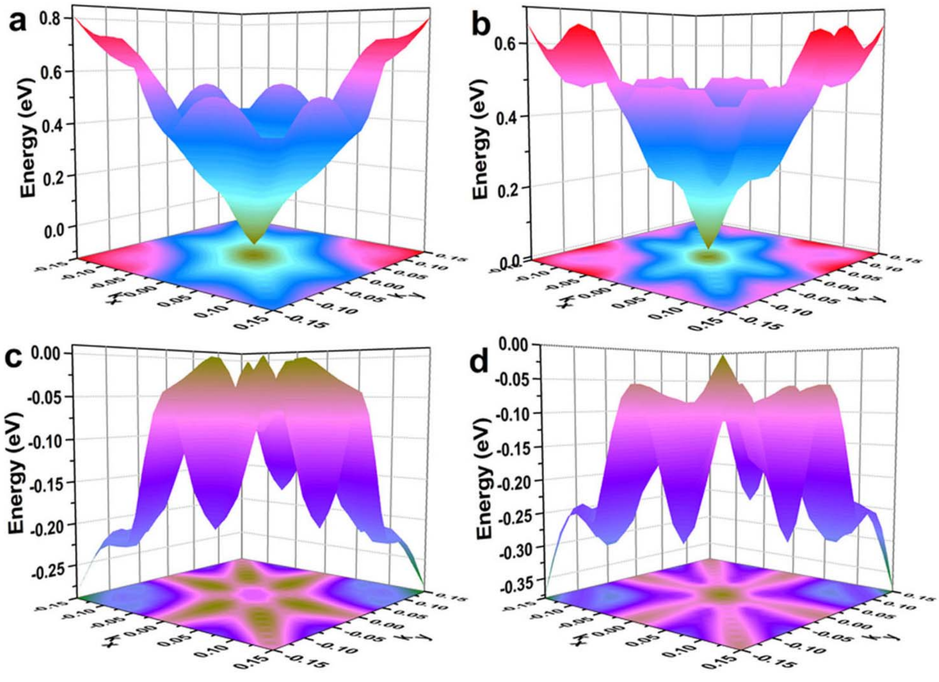

Figure 4 | **Comparison of the Dirac cone around the Γ point for $(Bi_{1-x}Sb_x)_2Te_3$ with $x = 0$ and $x = 1$.** (a) and (b) the upper Dirac cone for $x = 0$ and $x = 1$, and (c) and (d) the lower Dirac cone for $x = 0$ and $x = 1$, respectively. The constant-energy contour plots are given at the bottom.

Table 1 | The formation energies E_f (eV) for different sites of vacancies (V_{Te1} and V_{Te2}) and antisite defects (Te_{Bi}) in 15-atom and 40-atom $(Bi_1Sb_0)_2Te_3$ at the Te-rich and Te-poor conditions including spin-orbit coupling

		E_f (eV)						
Defect	Condition	15-1	15-2	15-3	15-4	15-5	15-6	40-atom
V_{Te2}	Te-rich	1.185	1.186	1.194	-	-	-	1.054
	Te-poor	0.862	0.863	0.871	-	-	-	0.731
V_{Te1}	Te-rich	0.831	0.826	0.803	0.798	0.826	0.804	0.956
	Te-poor	0.508	0.503	0.480	0.475	0.503	0.481	0.633
Te_{Bi}	Te-rich	0.309	0.311	0.309	0.485	0.312	0.310	0.396
	Te-poor	1.117	1.119	1.117	1.293	1.120	1.118	1.204

electron-type bulk carries and realize a more insulating bulk. However, for the Te_{Bi} formation energies, the situation is drastically different. The Te-rich condition leads to the lower formation energy, meaning more electron-type bulk carries induced by Te_{Bi}. Calculations of the formation energies of V_{Te1}, V_{Te2}, and Te_{Bi} using the 40-atom $(Bi_1Sb_0)_2Te_3$ show the similar results (**Table 1**). Therefore, controlling the growth or annealing conditions is not an effective way to reduce the bulk carrier density.

For the solid-solution $(Bi_{1-x}Sb_x)_2Te_3$, the most stable configuration at a given Sb concentration x is used. **Fig. 5a** presents the formation energies of the lowest-energy V_{Te1} and Te_{Bi} with x=0 and x=1/6 and that of Sb_{Te} with x=1 and x=1/6 as a function of Te chemical potential. Obviously, when x increases from x = 0 to 1/6, both the formation energies of V_{Te1} and Te_{Bi} become larger for the entire range of Te chemical potentials, indicating that the formation of V_{Te1} and Te_{Bi} is much more difficult for x = 1/6 than that for x = 0, namely the bulk carrier density is reduced effectively. With increasing x, the SOC strength of $(Bi_{1-x}Sb_x)_2Te_3$ becomes smaller due to the weaker SOC of Sb than that of Bi. To see the effects of SOC strength on defects formation, formation energies of V_{Te1} and Te_{Bi} under rescaled SOC strength are calculated and the relative formation energies are plotted in **Figs. 5c** and **d**, respectively. It is quite remarkable that the relative formation energies of V_{Te1} and Te_{Bi} increase monotonically with decreasing SOC strength, which implies that the formation of V_{Te1} and Te_{Bi} becomes more difficult by the increasing Sb concentration x. This is in good agreement with the formation energies shown in **Fig. 5a**. In addition, it should be note that in a recent work[35] the formation energies of V_{Te1} and Te_{Bi} were calculated with neglect of SOC, and the values of both end conditions are larger than that of our results, which should compare to the tendency of **Figs. 5c** and **d**. However, for the case of Sb_{Te} as shown in **Fig. 5a**, the situation is rather different. The antisite defect Sb_{Te} in x=1 system is much more stable than that in x = 1/6 system though the x=1 system shows weaker SOC. Thus an available together factor exists. As shown in **Figs. 2c** and **d**, the lattice parameters *a* and *c* are effectively tuned with the x=1 system behaves the smallest ones. To

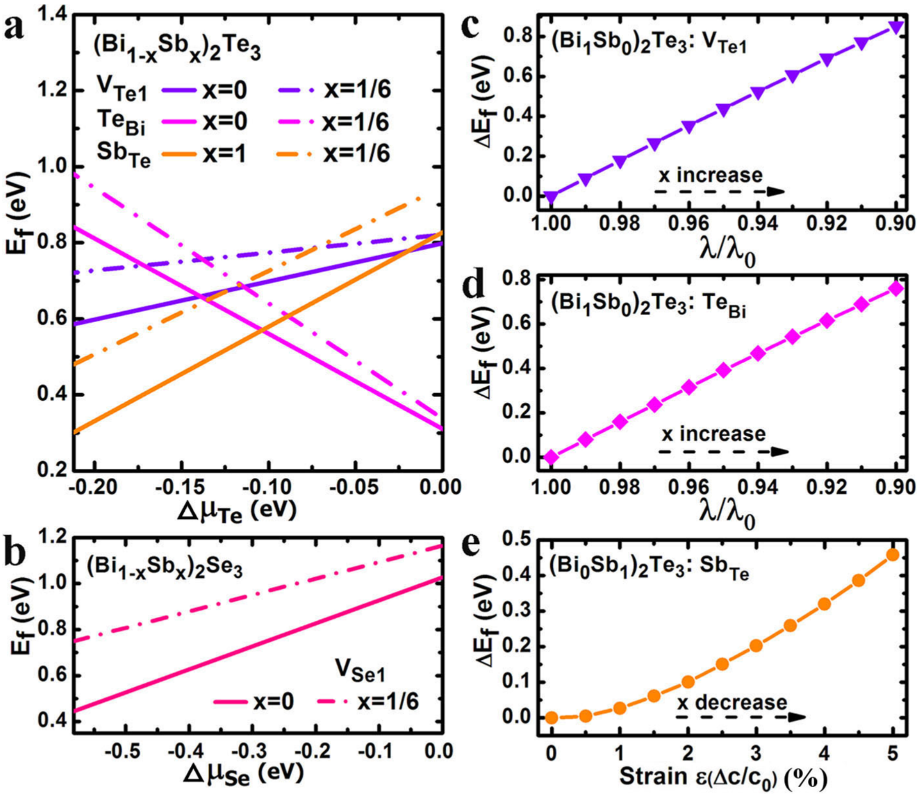

Figure 5 | Formation energies and relative formation energies. (a) Formation energies of the lowest-energy vacancy (V_{Te1}) and antisite (Te_{Bi} and Sb_{Te}) defects in $(Bi_{1-x}Sb_x)_2Te_3$ under various Te chemical potential (μ_{Te}), and (b) that of Vse1 in $(Bi_{1-x}Sb_x)_2Se_3$ under various μ_{Se}. (c) and (d) Relative formation energies of V_{Te1} and Te_{Bi} in $(Bi_1Sb_0)_2Te_3$ as a function of the SOC strength. The formation energy for the actual SOC strength ($\lambda/\lambda_0=1$) is set to zero. (e) Strain dependence of relative formation energy of Sb_{Te} in $(Bi_0Sb_1)_2Te_3$. c_0 refers to the lattice constants of the unstrained $(Bi_0Sb_1)_2Te_3$, and Δc to the difference of that between strained and unstrained systems.

investigate their effect, the isotropic strain is applied and strain dependence of relative formation energy of Sb_{Te} in $(Bi_0Sb_1)_2Te_3$ is plotted in **Fig. 5e**. It is found that the relative formation energy increases monotonically with increasing isotropic strain from 0 to 5%. Hence, the decreasing of the formation energy of Sb_{Te} is mainly determined by the effect of lattice parameters changes. In addition, we also study the native point defect (V_{Se}) in solid-solution $(Bi_{1-x}Sb_x)_2Se_3$ and the results show that the introducing of Sb is an effect way to reduce the bulk carrier density (**Fig. 5d**)[36]. In a word, the solid-solution is a novel promising pathway to eliminating the bulk states that depends on the changes of both the SOC and the lattice parameters.

Discussion

Systematic first-principles calculations are carried out to investigated the band structure engineering in $(Bi_{1-x}Sb_x)_2Te_3$. The effects of artificially rescaled SOC and lattice parameters are considered due to their changes caused by the increasing of Sb concentration. Our results can be summarized into three main points:

(1) The SOC of $(Bi_{1-x}Sb_x)_2Te_3$ is strong enough to invert the highest valence band and lowest conduction band over the entire range of x, indicating the robustness of bulk Z_2 topology.
(2) For the topological surface states, with decreasing SOC, i.e., increasing x, Dirac point moves upward to the bulk energy gap and Dirac fermion velocity v_D increases, resulting in the ideal Dirac point and a series of novel ternary topological insulators.
(3) The $(Bi_{1-x}Sb_x)_2Te_3$ ternary compounds have much more insulting bulk than the parents due to the formation of the native point defects is eliminated effectively that depends on both lattice changes and reduced SOC.

The highly insulating bulk and tunable Dirac cone have been achieved in $(Bi_{1-x}Sb_x)_2Te_3$, which is consistent with experimentally observation and is significant for the development of dissipationless devices based on the TIs.

Methods

All of the calculations, including geometry relaxation and electronic structure calculations, are performed using the projector augmented wave method with a plane-wave basis set as implemented in the Vienna ab initio simulation package (VASP) code[37]. The plane wave cutoff energy is 400 eV and the exchange correlation functional is treated by Perdew–Burke–Ernzerhof from generalized gradient approximation (GGA)[38]. For the Brillouin-zone sampling, a Γ-centered $7\times7\times5$ Monkhorst-Pack k mesh is used for 15-atom conventional cell, a $5\times5\times5$ k mesh for the 40-atom rhombohedral supercell, and a $15\times15\times1$ k mesh for the five QLs. Both a 40-atom supercell and a 15-atom conventional cell are used for the bulk investigation[30] and a slab of five quintuple layers (QLs) with the vacuum layer of 20 Å to avoid interactions between adjacent slabs for the (111) surface[27]. The lattice parameters and all the atomic positions are fully relaxed until the residual forces on each atom are smaller than 0.001 eV/Å. SOC is invoked in the calculation on a fully self-consistent basis.

1. Moore, J. E. The birth of topological insulators. *Nature (London)* **464**, 194–198 (2010).
2. Hasan, M. & Kane, C. Colloquium: Topological insulators. *Rev. Mod. Phys.* **82**, 3045–3067 (2010).
3. Qi, X.-L. & Zhang, S.-C. Topological insulators and superconductors. *Rev. Mod. Phys.* **83**, 1057–1110 (2011).
4. Bernevig, B. A., Hughes, T. L. & Zhang, S. C. Quantum spin Hall effect and topological phase transition in HgTe quantum wells. *Science* **314**, 1757–1761 (2006).
5. Zhang, H. *et al.* Topological insulators in Bi_2Se_3, Bi_2Te_3 and Sb_2Te_3 with a single Dirac cone on the surface. *Nat. Phys.* **5**, 438–442 (2009).
6. Xia, Y. *et al.* Observation of a large-gap topological-insulator class with a single Dirac cone on the surface. *Nat. Phys.* **5**, 398–402 (2009).
7. Chen, Y. L. *et al.* Experimental realization of a three-dimensional topological insulator, Bi_2Te_3. *Science* **325**, 178–181 (2009).
8. Hsieh, D. *et al.* Observation of Time-Reversal-Protected Single-Dirac-Cone Topological-Insulator States in Bi_2Te_3 and Sb_2Te_3. *Phys. Rev. Lett.* **103**, 146401 (2009).
9. Fu, L. & Berg, E. Odd-Parity Topological Superconductors: Theory and Application to $Cu_xBi_2Se_3$. *Phys. Rev. Lett.* **105**, 097001 (2010).
10. Yu, R. *et al.* Quantized anomalous Hall effect in magnetic topological insulators. *Science* **329**, 61–64 (2010).
11. Chen, Y. L. *et al.* Massive Dirac Fermion on the Surface of a Magnetically Doped Topological Insulator. *Science* **329**, 659–662 (2010).
12. Park, K., Heremans, J., Scarola, V. & Minic, D. Robustness of Topologically Protected Surface States in Layering of Bi_2Te_3 Thin Films. *Phys. Rev. Lett.* **105**, 186801 (2010).
13. Zhang, Y. *et al.* Crossover of the three-dimensional topological insulator Bi_2Se_3 to the two-dimensional limit. *Nat. Phys.* **6**, 584–588 (2010).
14. Wray, L. A. *et al.* A topological insulator surface under strong Coulomb, magnetic and disorder perturbations. *Nat. Phys.* **7**, 32–37 (2011).
15. Niu, C. *et al.* Mn induced ferromagnetism and modulated topological surface states in Bi_2Te_3. *Appl. Phys. Lett.* **98**, 252502 (2011).
16. Hsieh, D. *et al.* A tunable topological insulator in the spin helical Dirac transport regime. *Nature (London)* **460**, 1101–1105 (2009).
17. Peng, H. *et al.* Aharonov-Bohm interference in topological insulator nanoribbons. *Nat. Mater.* **9**, 225–229 (2010).
18. Hor, Y. S. *et al.* p-type Bi_2Se_3 for topological insulator and low-temperature thermoelectric applications. *Phys. Rev. B* **79**, 195208 (2009).
19. Qu, D. X., Hor, Y. S., Xiong, J., Cava, R. J. & Ong, N. P. Quantum oscillations and hall anomaly of surface states in the topological insulator Bi_2Te_3. *Science* **329**, 821–824 (2010).
20. Chen, J. *et al.* Gate-Voltage Control of Chemical Potential and Weak Antilocalization in Bi_2Se_3. *Phys. Rev. Lett.* **105**, 176602 (2010).
21. Kong, D. *et al.* Few-layer nanoplates of Bi_2Se_3 and Bi_2Te_3 with highly tunable chemical potential. *Nano. Lett.* **10**, 2245–2250 (2010).
22. Steinberg, H., Gardner, D. R., Lee, Y. S. & Jarillo-Herrero, P. Surface State Transport and Ambipolar Electric Field Effect in Bi_2Se_3 Nanodevices. *Nano. Lett.* **10**, 5032–5036 (2010).
23. Checkelsky, J., Hor, Y., Cava, R. & Ong, N. Bulk Band Gap and Surface State Conduction Observed in Voltage-Tuned Crystals of the Topological Insulator Bi_2Se_3. *Phys. Rev. Lett.* **106**, 196801 (2011).
24. Xu, S. Y. *et al.* Topological phase transition and texture inversion in a tunable topological insulator. *Science* **332**, 560–564 (2011).
25. Sato, T. *et al.* Unexpected mass acquisition of Dirac fermions at the quantum phase transition of a topological insulator. *Nat. Phys.* **7**, 840–844 (2011).
26. Kong, D. *et al.* Ambipolar field effect in the ternary topological insulator $(Bi_xSb_{1-x})_2Te_3$ by composition tuning. *Nat. Nano.* **6**, 705–709 (2011).
27. Zhang, J. *et al.* Band structure engineering in $(Bi_{1-x}Sb_x)_2Te_3$ ternary topological insulators. *Nat. Commun.* **2**, 574 (2011).
28. Ren, Z., Taskin, A., Sasaki, S., Segawa, K. & Ando, Y. Optimizing $Bi_{2-x}Sb_xTe_{3-y}Se_y$ solid solutions to approach the intrinsic topological insulator regime. *Phys. Rev. B* **84**, 165311 (2011).
29. Arakane, T. *et al.* Tunable Dirac cone in the topological insulator $Bi_{2-x}Sb_xTe_{3-y}Se_y$. *Nat. Commun.* **3**, 636 (2012).
30. Thonhauser, T., Jeon, G., Mahan, G. & Sofo, J. Stress-induced defects in Sb_2Te_3. *Phys. Rev. B* **68**, 205207 (2003).
31. Vegard, L. Die Konstitution der Mischkristalle und die Raumfüllung der Atome. *Z. Phys.* **5**, 17–26 (1921).
32. Eremeev, S. V. *et al.* Atom-specific spin mapping and buried topological states in a homologous series of topological insulators. *Nat. Commun.* **3**, 635 (2012).
33. Zhang, J. L. *et al.* Pressure-induced superconductivity in topological parent compound Bi_2Te_3. *Proc. Natl. Acad. Sci. U. S. A.* **108**, 24–28 (2011).
34. Zhang, S. B. & Northrup, J. E. Chemical potential dependence of defect formation energies in GaAs: Application to Ga self-diffusion. *Phys. Rev. Lett.* **67**, 2339–2342 (1991).
35. Hashibon, A. & Elsässer, C. First-principles density functional theory study of native point defects in Bi_2Te_3. *Phys. Rev. B* **84**, 144117 (2011).
36. Hong, S. S., Cha, J. J., Kong, D. & Cui, Y. Ultra-low carrier concentration and surface-dominant transport in antimony-doped Bi_2Se_3 topological insulator nanoribbons. *Nat. Commun.* **3**, 757 (2012).
37. Kresse, G. & Furthmüller, J. Efficient iterative schemes for ab initio total-energy calculations using a plane-wave basis set. *Phys. Rev. B* **54**, 11169–11186 (1996).
38. Perdew, J. P., Burke, K. & Ernzerhof, M. Generalized Gradient Approximation Made Simple. *Phys. Rev. Lett.* **77**, 3865–3868 (1996).

Acknowledgements

This work is supported by the National Basic Research Program of China (973 program, 2013CB632401), National Science foundation of China under Grant number 11174180, 20973102, and 10974118, and the Natural Science Foundation of Shandong Province under Grant number ZR2011AM009, the ministry of education academic award for postgraduates. We also thank the National Supercomputer Center in Jinan for providing high performance computation.

Author contributions

Y.D. and B.B.H. designed the research. The density functional theory calculations were performed by C.W.N. and Y.T.Z. C.W.N. and Y.D. prepared the manuscript. All authors contributed to the scientific discussions.

Additional information

Supplementary information accompanies this paper at http://www.nature.com/scientificreports

Competing financial interests: The authors declare no competing financial interests.

How to cite this article: Niu, C. *et al*. Realization of tunable Dirac cone and insulating bulk states in topological insulators $(Bi_{1-x}Sb_x)_2Te_3$. *Sci. Rep.* **2**, 976; DOI:10.1038/srep00976 (2012).